JOURNAL OF SPACECRAFT AND ROCKETS
Vol. 34, No. 1, January–February 1997

Numerical Investigation of Supersonic Base Flow with Base Bleed

Jubaraj Sahu* and Karen R. Heavey†
U.S. Army Research Laboratory, Aberdeen Proving Ground, Maryland 21005-5066

A zonal, implicit, time-marching Navier–Stokes computational technique has been used to compute the turbulent supersonic base flow over a cylindrical afterbody with base bleed. A critical element of calculating such flows is the turbulence model. Two eddy viscosity turbulence models have been used in the base region flow computations. These models include an algebraic turbulence model and a two-equation k–ϵ model. The k–ϵ equations are solved using an implicit algorithm, and calculations with the k–ϵ model are extended up to the wall. Flowfield computations have been performed for a cylindrical afterbody at $M = 2.46$ and at an angle of attack of $\alpha = 0$ deg. The results are compared with the experimental data for the same conditions and the same configuration. Details of the mean flowfield as well as the turbulence quantities have been presented. In addition, the computed base pressure distribution has been compared with the experiment. In general, the k–ϵ turbulence model performs better in the near wake than the algebraic model and predicts the base pressure much better.

Introduction

ONE of the important parameters in the design of a projectile is the total aerodynamic drag. The total drag consists of three drag components: the pressure drag or the wave drag (excluding the base), the viscous drag, and the base drag. The base drag component is a large part of the total drag and can be as high as 50% or more of the total drag. Of all these three components of drag, the most difficult one to predict is the base drag. The base drag depends on the pressure acting on the base, and therefore it is necessary to predict the base pressure as accurately as possible.

The ability to compute the base region flowfield for projectile configurations using Navier–Stokes computational techniques has been developed over the past few years.[1–3] Recently, improved numerical predictions have been obtained using a more advanced zonal upwind flux-split algorithm.[4,5] This zonal scheme preserves the base corner and allows better modeling of the base region flow. These studies have included base flows for different base geometries. This capability is very important for determining aerodynamic coefficient data including the total aerodynamic drag. As indicated earlier, a number of base flow calculations have been made, and base drag and total drag have been predicted with reasonable accuracy. However, due to the lack of available data, the predictive capabilities were not assessed earlier with detailed base pressure distributions, mean flow velocity components, and turbulence quantities. This situation is especially true of base flow for axisymmetric bodies at transonic and supersonic speeds. Recently, experimental measurements have been made in the base region for supersonic flow over a cylindrical afterbody without base bleed.[6] The data included the base pressure distribution (along the base), mean flow, and turbulence quantities. Numerical computations[7] were made for this case, and computed results were compared with these data. The detailed experimental data were critical in the validation of the computational results, especially for the turbulence modeling and grid resolution issues.

Figure 1 is a schematic diagram showing the important features of supersonic base flow with base bleed. The approaching supersonic turbulent boundary layer separates at the base corner, and the free shear layer region is formed in the wake. The flow expands at the base corner and is followed by the recompression shock downstream of the base, which realigns the flow. The flow then redevelops in the trailing wake. In the absence of base bleed, a low-pressure region is formed immediately downstream of the base, which is characterized by a low-speed recirculating flow region. Interaction between this recirculating region and the inviscid external flow occurs through the free shear mixing region. This mixing region is where turbulence plays an important role. Injection of low-speed air into the base region displaces the entire recirculation region downstream into the wake. The bleed flow weakens the recompression shock, resulting in an increase of base pressure or a reduction in base drag.

The drag reduction due to base bleed at supersonic speeds is of practical importance. The effect of base bleed or mass injection has been studied experimentally.[8–10] These early experiments involved cold and hot gas injection for cylindrical and boat-tailed afterbodies and clearly showed the effectiveness of base bleed on base pressure. Most of these experimental investigations were rather limited in nature and lacked measurements of the detailed base pressure distribution and near-wake flowfield such as mean flow and turbulence quantities. Such detailed experimental data have been made available recently for supersonic flow over a cylindrical afterbody with base bleed.[11] This set of experimental data not only provides insight into the details of the fluid dynamic interactions in the near wake but also serves as a benchmark for validation of computational results. This paper describes the computational investigation of supersonic base flow with base bleed for the same experimental model and conditions.

The basic configuration used in this study is a cylindrical afterbody. As mentioned earlier, a simple composite grid scheme has been used for accurate modeling of the base corner. Numerical flowfield computations have been performed at $M_\infty = 2.46$ and at 0-deg angle of attack. Two turbulence models (an algebraic model and a two-equation model) are used in the base flow region. All of the computations have been performed on the Cray Y-MP supercomputer. Details of the flowfield, such as Mach number contours and base pressure distributions, are presented. Computed base pressure distributions are compared with available experimental data for the same conditions and the same configuration.

Governing Equations and Solution Technique

The complete set of time-dependent, Reynolds-averaged, thin-layer Navier–Stokes equations is solved numerically to obtain a solution to this problem. The numerical technique used is an implicit, finite difference scheme. Although time-dependent calculations are made, the transient flow is not of primary interest at the present time. The steady flow, which is the desired result, is obtained in a time asymptotic fashion.

Governing Equations

The complete set of three-dimensional, time-dependent, generalized geometry, Reynolds-averaged, thin-layer, Navier–Stokes

---

Received Nov. 13, 1995; revision received July 15, 1996; accepted for publication Oct. 5, 1996. This paper is declared a work of the U.S. Government and is not subject to copyright protection in the United States.

*Aerospace Engineer, Aerodynamics Branch. Associate Fellow AIAA.

†Mathematician, Aerodynamics Branch.

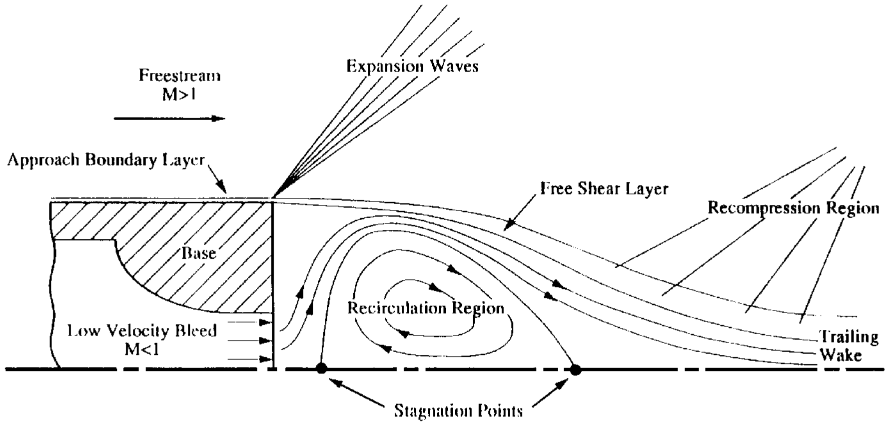

Fig. 1 Schematic diagram of supersonic base flow.

equations for general spatial coordinates ξ, η, and ζ can be written as follows[12]:

$$\partial_T \hat{\boldsymbol{q}} + \partial_\xi \hat{\boldsymbol{F}} + \partial_\eta \hat{\boldsymbol{G}} + \partial_\zeta \hat{\boldsymbol{H}} = Re^{-1} \partial_\zeta \hat{\boldsymbol{S}} \tag{1}$$

where

ξ = longitudinal coordinate, $\xi(x, y, z, t)$
η = circumferential coordinate, $\eta(x, y, z, t)$
ζ = nearly normal coordinate, $\zeta(x, y, z, t)$
T = time, t

In Eq. (1), $\hat{\boldsymbol{q}}$ contains the dependent variables and $\hat{\boldsymbol{F}}$, $\hat{\boldsymbol{G}}$, and $\hat{\boldsymbol{H}}$ are flux vectors. The thin-layer approximation is used here, and the viscous terms involving velocity gradients in both the longitudinal and circumferential directions are neglected. The viscous terms are retained in the normal direction ζ and are collected into the vector $\hat{\boldsymbol{S}}$. These viscous terms are used everywhere. However, in the wake or the base region, similar viscous terms are also added in the streamwise direction. For this computation, the diffusion coefficients μ and κ contain molecular and turbulent parts. The turbulent contributions are supplied through either an algebraic or a two-equation k–ϵ turbulence model.

Numerical Technique

The implicit, approximately factored scheme for the thin-layer Navier–Stokes equations using central differencing in the η and ζ directions and upwinding in ξ is written in the following form:

$$\begin{aligned}
&\left[\boldsymbol{I} + h\delta_\xi^b (\hat{\boldsymbol{A}}^+)^n + h\delta_\zeta \hat{\boldsymbol{C}}^n - hRe^{-1}\bar{\delta}_\zeta J^{-1}\hat{\boldsymbol{M}}^n J - \boldsymbol{D}_i\Big|_\zeta\right] \\
&\quad \times \left[I + h\delta_\xi^f (\hat{\boldsymbol{A}}^-)^n + h\delta_\eta \hat{\boldsymbol{B}}^n - \boldsymbol{D}_i\Big|_\eta\right]\Delta\hat{\boldsymbol{Q}}^n \\
&\quad = -\Delta t\Big\{\delta_\xi^b\left[(\hat{\boldsymbol{F}}^+)^n - \hat{\boldsymbol{F}}_\infty^+\right] + \delta_\xi^f\left[(\hat{\boldsymbol{F}}^-)^n - \hat{\boldsymbol{F}}_\infty^-\right] + \delta_\eta\left(\hat{\boldsymbol{G}}^n - \hat{\boldsymbol{G}}_\infty\right) \\
&\quad + \delta_\zeta\left(\hat{\boldsymbol{H}}^n - \hat{\boldsymbol{H}}_\infty\right) - Re^{-1}\bar{\delta}_\zeta\left(\hat{\boldsymbol{S}}^n - \hat{\boldsymbol{S}}_\infty\right)\Big\} - \boldsymbol{D}_e\left(\hat{\boldsymbol{Q}}^n - \hat{\boldsymbol{Q}}_\infty\right)
\end{aligned} \tag{2}$$

where $h = \Delta t$ or $(\Delta t)/2$. Here, δ is typically a three-point second-order accurate central difference operator, $\bar{\delta}$ is a midpoint operator used with the viscous terms, and the operators δ_ξ^b and δ_ξ^f are backward and forward three-point difference operators. The flux $\hat{\boldsymbol{F}}$ has been eigensplit, and the matrices $\hat{\boldsymbol{A}}$, $\hat{\boldsymbol{B}}$, $\hat{\boldsymbol{C}}$, and $\hat{\boldsymbol{M}}$ result from local linearization of the fluxes about the previous time level. Here, J denotes the Jacobian of the coordinate transformation. Dissipation operators $\boldsymbol{D}_e$ and $\boldsymbol{D}_i$ are used in the central space differencing directions. The smoothing terms used in the present study are of the form

$$\boldsymbol{D}_e|_\eta = (\Delta t)J^{-1}\left\{\epsilon_2\bar{\delta}\rho(\boldsymbol{B})\beta\bar{\delta} + \epsilon_4\bar{\delta}[\rho(\boldsymbol{B})/(1+\beta)]\bar{\delta}^3\right\}\Big|_\eta J$$

$$\boldsymbol{D}_i|_\eta = (\Delta t)J^{-1}\left[\epsilon_2\bar{\delta}\rho(\boldsymbol{B})\beta\bar{\delta} + 2.5\epsilon_4\bar{\delta}\rho(\boldsymbol{B})\bar{\delta}\right]|_\eta J$$

where

$$\beta = \frac{|\bar{\delta}^2 P|}{|(1+\delta^2)P|}$$

and where $\rho(\boldsymbol{B})$ is the true spectral radius of $\boldsymbol{B}$. The idea here is that the fourth-order difference will be tuned down near shocks (e.g., as β gets large, the weight on the fourth-order difference drops down, whereas the second-order difference tunes up).

Boundary Conditions

For simplicity, most of the boundary conditions have been imposed explicitly.[3] An adiabatic wall boundary condition is used on the body surface, and the no-slip boundary condition is used at the wall. The pressure at the wall is calculated by solving a combined momentum equation. Freestream boundary conditions are used at the inflow boundary as well as at the outer boundary. A symmetry boundary condition is imposed at the cirumferential edges of the grid, whereas a simple extrapolation is used at the downstream boundary. A combination of a symmetry and extrapolation boundary condition is used at the centerline (axis). Since the freestream flow is supersonic, a nonreflection boundary condition is used at the outer boundary. The flowfield is initially set to freestream conditions everywhere and then advanced in time until a steady-state solution is obtained.

For the base bleed case, boundary conditions are imposed at the bleed exit that include the total temperature and total pressure of the bleed gas as well as a mass injection parameter I. The amount of gas injection is usually defined in terms of the mass injection parameter, $I = \dot{m}_j/\rho_\infty u_\infty A_b$, where $\dot{m}_j$ is the mass flow at the bleed exit and A_b is the area at the base. All dependent flow variables can be determined from these three quantities for the mass injection or base bleed case. The total pressure and temperature of injected gas are assumed to be constant at the bleed exit.

Composite Grid Scheme

In the present work, a simple composite grid scheme has been used where a large single grid is split into a number of smaller grids so that computations can be performed on each grid separately.[5] These grids use the available core memory one grid at a time. The remaining grids are stored on an external disk storage device. Some of today's supercomputers have a large incore memory to fit the large single grid. However, for accurate geometric modeling of complex projectile configurations that include blunt noses, sharp corners, and base cavities, it is also desirable to split the large database into a few smaller zones. The use of a composite grid scheme requires special care in storing and fetching the interface boundary data (i.e., the communication between the various zones). In the present scheme, there is a one-to-one mapping of the grid points at the interface boundaries. Thus, no interpolations are required. Details of the data storage, data transfer, and other pertinent information, such as metric and differencing accuracy at the interfaces, can be found in the work of Sahu and Nietubicz.[5]

Turbulence Modeling

For the base flow calculations, two turbulence models have been used. The first one is an algebraic eddy viscosity model (Baldwin–Lomax model). The other one is a two-equation k–ϵ turbulence model that is also an eddy viscosity model.

Baldwin–Lomax Model

This model is the one developed by Baldwin and Lomax.[13] It is a two-layer model in which an eddy viscosity is calculated for an inner and an outer region. The inner region follows the Prandtl–Van Driest formulation. In both the inner and outer formulations, the distribution of vorticity is used to determine the length scales, thereby avoiding the necessity of finding the outer edge of the boundary layer. For the inner region,

$$(\mu_t)_{\text{inner}} = \rho l^2|\omega| \tag{3}$$

where

$$l = \kappa y\left[1 - \exp\left(\frac{-y^+}{A^+}\right)\right]$$

$$y^+ = \frac{\rho_W u_T y}{\mu_W}, \qquad u_T = \sqrt{\left(\frac{T_W}{\rho_W}\right)}$$

and $|\omega|$ is the absolute magnitude of vorticity. The eddy viscosity for the outer region is given by

$$(\mu_t)_{\text{outer}} = KC_{cp}\rho F_{\text{wake}}F_{\text{kleb}}(y) \tag{4}$$

where $F_{\text{wake}} = y_{\max}F_{\max}$ or $C_{\text{wk}}y_{\max}u^2_{\text{dif}}/F_{\max}$; the smaller of the two values is used. The quantities $y_{\max}$ and $F_{\max}$ are determined from the function $F(y) = y, \omega, [1-\exp(-y^+/A^+)]$, where $F_{\max}$ is the maximum value of $F(y)$ and $y_{\max}$ is the value of y at which it occurs. The function $F_{\text{kleb}}(y)$ is the Klebanoff intermittency factor. The quantity u_{dif} is the difference between the maximum and minimum total velocity in the profile, and, for boundary layers, the minimum is zero.

The outer formulation can be used in wakes as well as in attached and separated boundary layers. For free-shear layer flow regions or wakes, the Van Driest damping term $[\exp(-y^+/A^+)]$ is neglected. Also, for the base or wake region, the distance y is measured from the centerline of symmetry. It is necessary to specify the following constants: $A^+ = 26$, $C_{\text{cp}} = 1.6$, $C_{\text{kleb}} = 0.3$, $C_{\text{wk}} = 0.25$, $\kappa = 0.4$, and $K = 0.0168$. This type of simple model is generally inadequate for complex flows containing flow separation regions such as base flow because it depends only on local information. The two-equation model contains less empiricism and allows the flow history to be taken into account.

Two-Equation k–ϵ Model

The two-equation turbulence model used here is Chien's k–ϵ model,[14] which is similar to that of Jones and Launder.[15] In this model, two transport equations are solved for the two variables k (turbulent kinetic energy) and ϵ (turbulent dissipation rate):

$$\begin{aligned}
\rho\frac{\mathrm{D}k}{\mathrm{D}t} &= \frac{\partial}{\partial X_j}\left[\left(\frac{\mu_t}{\sigma_k}+\mu\right)\frac{\partial k}{\partial X_j}\right] \\
&\quad + \mu_t\frac{\partial u_i}{\partial X_j}\left(\frac{\partial u_i}{\partial X_j}+\frac{\partial u_j}{\partial X_i}\right) - \rho\epsilon - 2\mu\frac{k}{y_n^2} \\
\rho\frac{\mathrm{D}\epsilon}{\mathrm{D}t} &= \frac{\partial}{\partial X_j}\left[\left(\frac{\mu_t}{\sigma_\epsilon}+\mu\right)\frac{\partial \epsilon}{\partial X_j}\right] + c_1\mu_t\frac{\epsilon}{k}\frac{\partial u_i}{\partial X_j} \\
&\quad \times\left(\frac{\partial u_i}{\partial X_j}+\frac{\partial u_j}{\partial X_i}\right) - c_2\rho\frac{\epsilon^2}{k} - 2\mu\frac{\epsilon}{y_n^2}e^{-y^+/2}
\end{aligned} \tag{5}$$

Here, y_n is the distance normal to the surface. The coefficients in the k and ϵ equations are given by

$$c_1 = 1.44, \qquad c_2 = 1.92\left[1 - 0.3\exp\left(-R_t^2\right)\right]$$

$$c_3 = 2.0, \qquad \sigma_k = 1.0, \qquad \sigma_\epsilon = 1.3$$

$$c_\mu = 0.09[1 - \exp(-0.01y^+)]$$

where $R_t = k^2/\nu\epsilon$. A compressibility correction[16] is applied to the k equation and ϵ is replaced by $\epsilon(1 + M_t^2)$, where $M_t^2 = 2k/T$. The k–ϵ model employs the eddy viscosity concept and relates the turbulent eddy viscosity to k and ϵ by

$$\mu_t = c_\mu\rho(k^2/\epsilon) \tag{6}$$

Following the same procedure used for the mean flow equations, the turbulence field equations are written in conservation form and then transformed into generalized coordinates.[17]

Model Geometry and Experiment

The computational accuracy of a numerical scheme can be established through comparisons with available experimental data. The model used in the experiment[11] and in the computational study is shown in Fig. 2. It is an axisymmetric cylindrical afterbody that has a diameter of 63.5 mm and a base bleed jet exit diameter of 25.4 mm. This figure also shows the location of the static pressure taps where base pressure was measured. The same configuration is used in the numerical simulations for a direct comparison.

Experimental measurements for this model have been made at the University of Illinois supersonic wind tunnel,[11] which was specifically designed for the study of axisymmetric base flows. The model was tested at 0-deg angle of attack, Mach number of 2.46, and Reynolds number of 5.21 × 10^7/m. In addition to measuring the velocity components at a number of selected longitudinal positions in the wake or base region, the base pressure was measured at 10 positions along the base. Such detailed base pressure measurements have not been made in the past for the base bleed condition and are very helpful in the code validation process. The velocity profile is

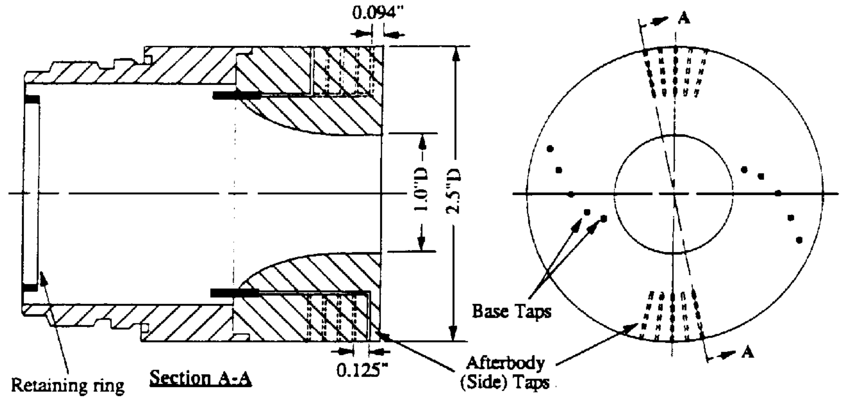

Fig. 2 Afterbody measurement locations.

also measured at a station upstream of the base that provides the upstream boundary condition for base region flowfield calculations.

Results

Numerical computations have been made for the cylindrical afterbody at a Mach number of 2.46 and at 0-deg angle of attack. The three-plane version of the three-dimensional code was run for the 0-deg angle-of-attack case. Two end planes were used to specify symmetric boundary conditions in the circumferential plane.

The solution technique requires the discretization of the entire flow region of interest into a suitable computational grid. The grid outer boundary has been placed 1 diameter away from the surface of the afterbody. The downstream boundary was placed 10 diameters away from the base. Because the calculations are in the supersonic regime, the computational outer boundary was placed close to the body, and a nonreflection boundary condition was used at that boundary. Figure 3 shows an expanded view of the grid in the base region. The surface points on the afterbody and the base were obtained first. These points were then used as inputs for obtaining the full grid using an algebraic grid generation program. The full grid is split into two zones, one upstream of the base and the other one in the base region or the wake. These grids consist of 22×60 and 94×119 grid points, respectively. Figure 3 shows the longitudinal grid clustering near the base corner. Grid points are also clustered near the afterbody surface to capture the viscous effects in the turbulent boundary layer. The clustered grid points are spread out downstream of the base in the wake to capture the free shear layer region. As part of a grid resolution study, two other grids were considered. One was a coarse grid with half as many grid points in the streamwise direction, and the other one was a fine grid consisting of twice as many grid points as the original grid described earlier. The results are presented later in this section. For the 0-deg angle-of-attack case considered, the grid was rotated circumferentially 5 deg on either side of the midplane. This rotation provided the three planes needed in the code to use central finite differences in the circumferential direction. In each case, the solution was marched from freestream conditions everywhere until the final converged solution was obtained. The results are now presented for both mean and turbulence quantities. Comparison of the computed results are made with the available experimental data.[11]

A few qualitative results are presented next. Figures 4a and 4b show computed Mach number contours of the base region flowfield for $I = 0$ (no bleed) and $I = 0.01$, respectively. The results show the flow expansion at the base corner and the recompression shock downstream of the base (coalescence of contour lines). In addition, Figs. 4a and 4b show the free shear layer in the near wake. Although not indicated in Fig. 4a, the flow in the near wake is primarily subsonic. For the zero bleed case, the usual wake narrowing (neck) can be clearly seen in the computed results and is followed by a strong recompression shock wave system. With base bleed, the expansion at the base corner weakens, the shear layer angle is decreased, and the recompression shock is very weak. The widening of the wake with injection ($I = 0.01$) can be observed in the computed results. The recirculatory flowfield in the near wake for the zero bleed case is displaced downstream with mass injection. The computed results shown in Fig. 4 were obtained using the two-equation k–ϵ model and the original grid.

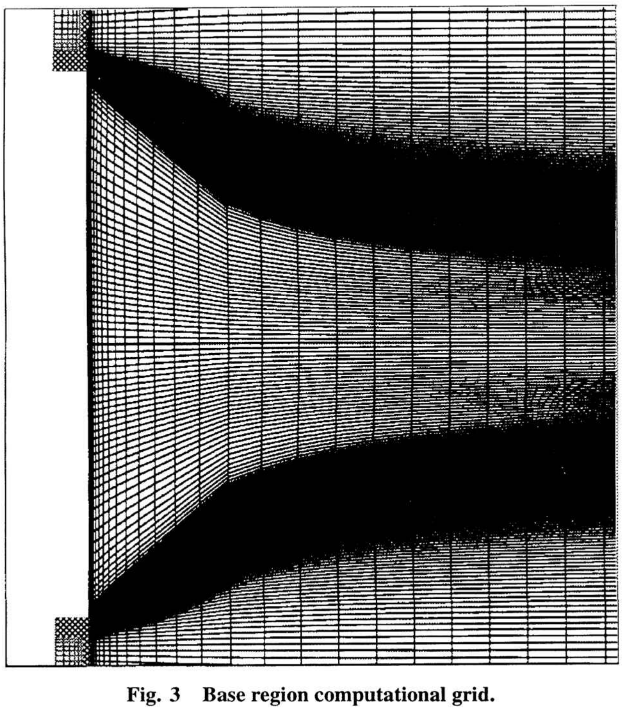

Fig. 3 Base region computational grid.

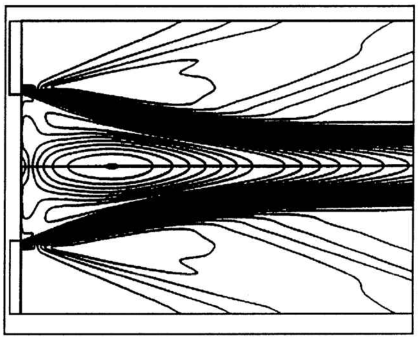

a) $I = 0.0$

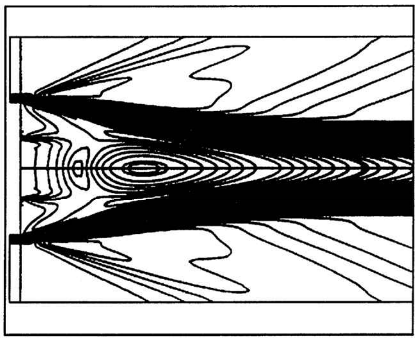

b) $I = 0.01$

Fig. 4 Computed Mach contours; $m_\infty = 2.46$ and $\alpha = 0$.

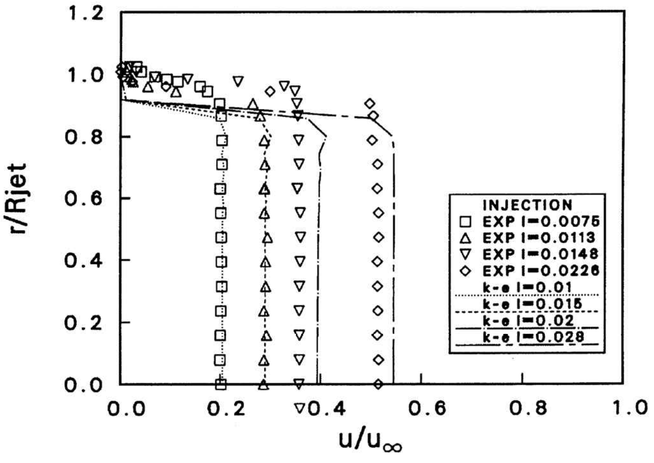

Fig. 5 Mean axial velocity distributions at bleed exit; $M_\infty = 2.46$, $\alpha = 0$ and k–ϵ model.

Figure 5 shows the velocity profiles at the base bleed exit plane for various mass injection rates. The mass injection rates selected for the numerical computations were initially based on the experiment. However, the experiment was later rerun to provide detailed measurements in the near wake. As it turned out, the injection rates obtained in the experimental data were slightly different from those used in the computation. Both computed and experimental results show the same trends. The exit velocity is quite uniform along the bleed exit. As expected, the magnitude of the exit velocity increases with an increase in the mass injection rate. There is some discrepancy in velocity near the bleed orifice corner. This is due in part to the grid point distribution in this area. The grid points were not clustered in this region because the flow inside the bleed hole and, thus, the boundary layer are not modeled. The effect of base bleed on the mean axial velocity along the centerline of symmetry is shown in Fig 6. The computed centerline velocity agrees fairly well with the experimental data in the near wake for $x/D < 3.0$. The agreement between the computed and experimental results is poor in the flow redevelopment region of the wake for all mass injection rates considered. In both the experimental and computed results, the bleed exit velocity is small for low injection rates and results in two stagnation points (forward and rear). The peak reverse velocity along the centerline decreases with an increase in the base bleed rate. As the mass injection rate is increased, the bleed exit velocity increases. The size of the recirculation region in the near wake is reduced and pushed farther downstream. For high injection rates ($I = 0.02$ or higher), reverse velocity does not exist along the centerline.

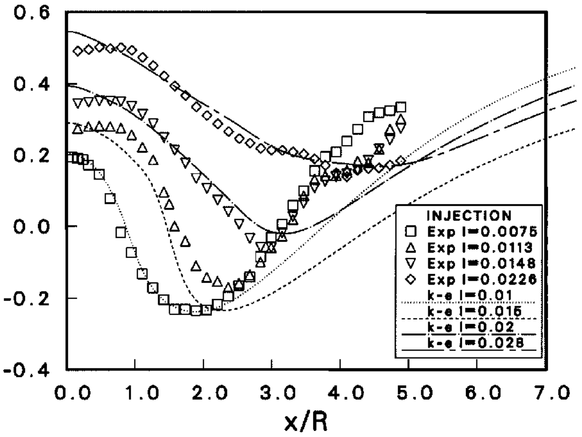

Fig. 6 Mean axial velocity along the centerline; M_∞ = 2.46, α = 0, and k–ϵ model.

Figures 7 and 8 show the velocity components in the streamwise and normal directions, respectively, for a mass injection parameter of $I = 0.01$. These velocity profiles are taken at four longitudinal positions in the wake or the base region ($X/D = 0.95$, 1.26, 1.67, and 2.04). The stations $X/D = 0.95$ and 1.67 correspond to the locations near the forward and rear stagnation points, respectively; $X/D = 1.26$ lies inside the recirculation region, and $X/D = 2.04$ is in the flow redevelopment region downstream of the rear stagnation point. The computed velocity profiles obtained using the Baldwin–Lomax algebraic turbulence model and the two-equation k–ϵ model are compared with the experimental data. Figure 7 shows the comparison of the u (streamwise) component of velocity. In general, the profiles obtained with the k–ϵ model are in better agreement with the experiment in the shear layer regions for $X/D = 0.95$ and 1.26. The profiles are poorly predicted by the algebraic model at these two stations. At $X/D = 0.95$, both turbulence models predict reverse velocities near the centerline that are larger than the experimental value, although the k–ϵ model prediction is closer to the experiment. The predicted profiles near the centerline agree better with the experimental data farther downstream ($X/D = 1.26$ and 1.67) inside the reverse flow region and near the rear stagnation point, especially the k–ϵ model prediction. Both models predict the velocity profiles at $X/D = 1.67$ and 2.04 fairly well. Figure 8 shows the comparison of the w (normal) component of the velocity. This component of velocity is better predicted by the k–ϵ model than the algebraic model in the near wake, especially at $X/D = 0.95$. The profiles predicted by the algebraic model are in poor agreement with the experimental data for radial positions greater than half of the base radius.

Some of the turbulence quantities are presented next. Figure 9 shows the turbulent kinetic energy profiles at the same longitudinal positions in the wake for the base bleed case, $I = 0.01$. The computed k profiles are obtained using the two-equation k–ϵ turbulence model. Near the forward stagnation point ($X/D = 0.95$) and inside the separated flow region ($X/D = 1.26$), the peak observed experimentally is well predicted by the k–ϵ model. Some discrepancy exists between the computed results and the experimental data for $r/R < 0.6$. The agreement of the computed profiles, including the location and magnitude of the peak, with the data is better near the rear stagnation point and downstream ($X/D = 1.67$ and 2.04), especially for the magnitude of the peak value. The radial

X/D = 0.95 *X/D* = 1.26

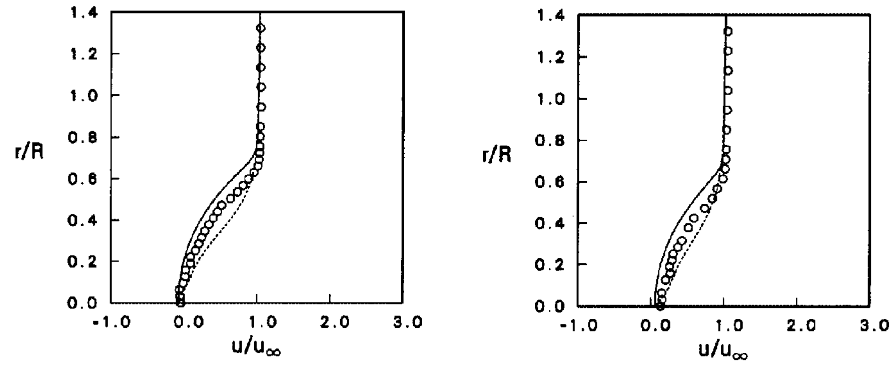

X/D = 1.67 *X/D* = 2.04

Fig. 7 Streamwise velocity (u) profiles; M_∞ = 2.46, α = 0, and I = 0.01: - - - -, B-L model; ——, k–ϵ model; and ○, experiment.

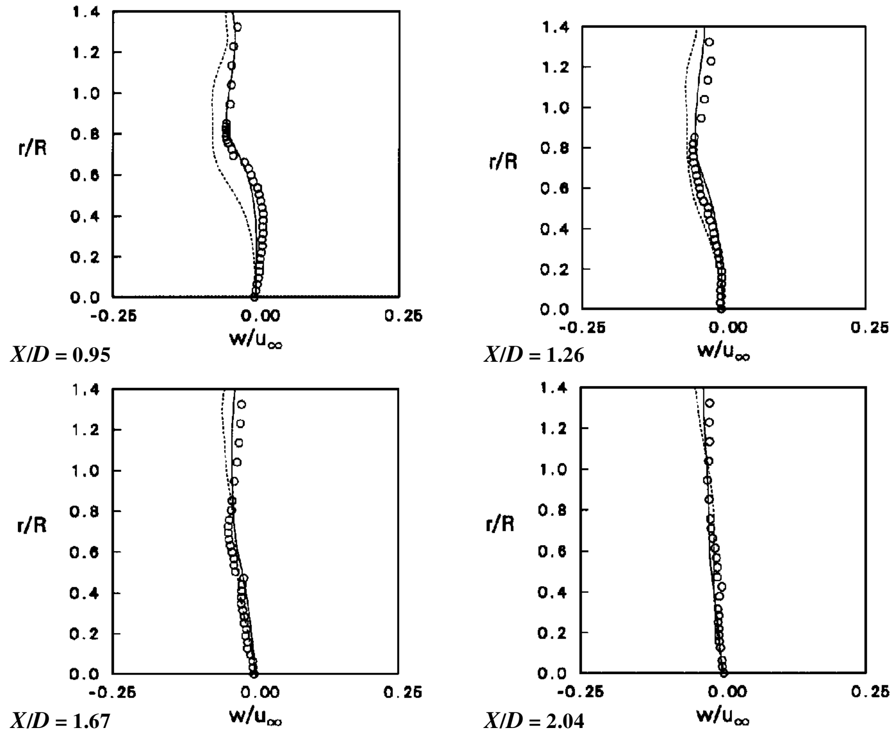

$X/D = 0.95$ $X/D = 1.26$

$X/D = 1.67$ $X/D = 2.04$

Fig. 8 Normal velocity (w) profiles; $M_\infty = 2.46$, $\alpha = 0$, and $I = 0.01$: - - - -, B-L model; ——, k–ϵ model; and ○, experiment.

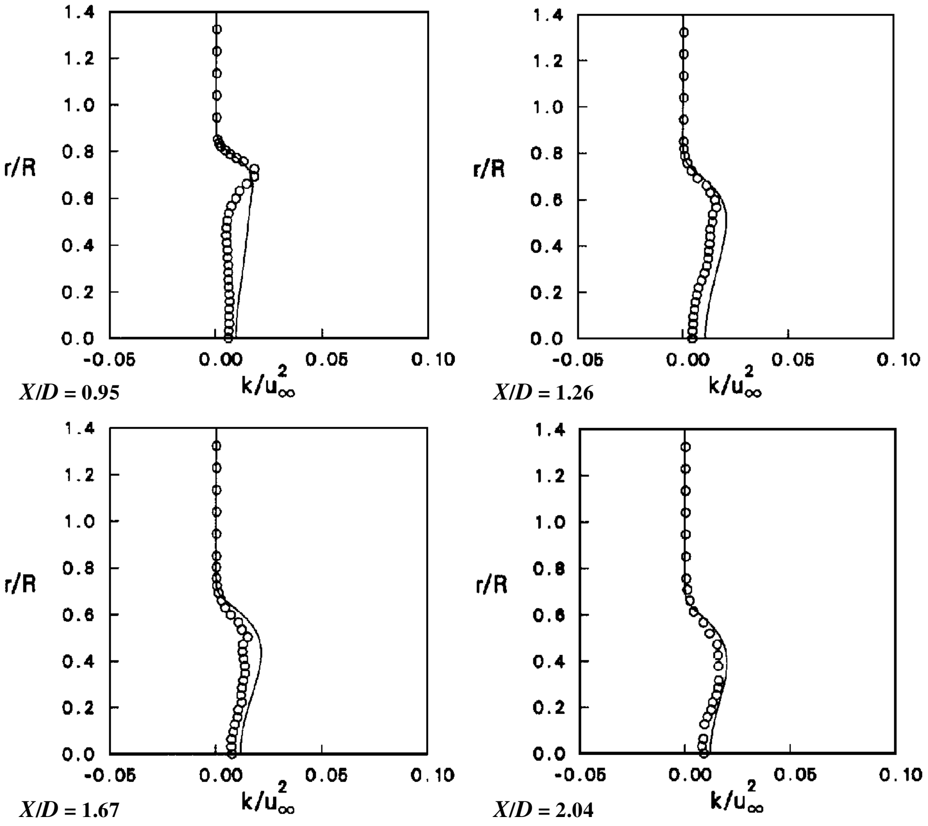

$X/D = 0.95$ $X/D = 1.26$

$X/D = 1.67$ $X/D = 2.04$

Fig. 9 Turbulent kinetic energy profiles; $M_\infty = 2.46$, $\alpha = 0$, and $I = 0.01$: ——, k–ϵ model; and ○, experiment.

location of the peaks decreases smoothly with increasing axial distance downstream from the base. Figure 10 shows the turbulent shear stress profiles in the near wake. The computed values obtained by both the algebraic model and the k–ϵ model are compared with the experimental data. In general, a small improvement can be observed in the predicted values with the k–ϵ model over the algebraic model. Discrepancy exists between the experimentally obtained turbulent shear stress and the predicted shear stresses with both turbulence models at $X/D = 0.95$ for $r/R < 0.7$. The location of the peak is better predicted by the k–ϵ model. The magnitude of the peak is well predicted by both models. For the other stations in the near wake, the magnitude of the peaks is predicted well by both models. As for the location of the peak, the k–ϵ model does much better than the algebraic model. As X/D is increased from 0.95 to 2.04, the location of the peak predicted by the k–ϵ model moves closer to the centerline similar to that observed in the experiment. The radial location of the peak is underpredicted by the algebraic model.

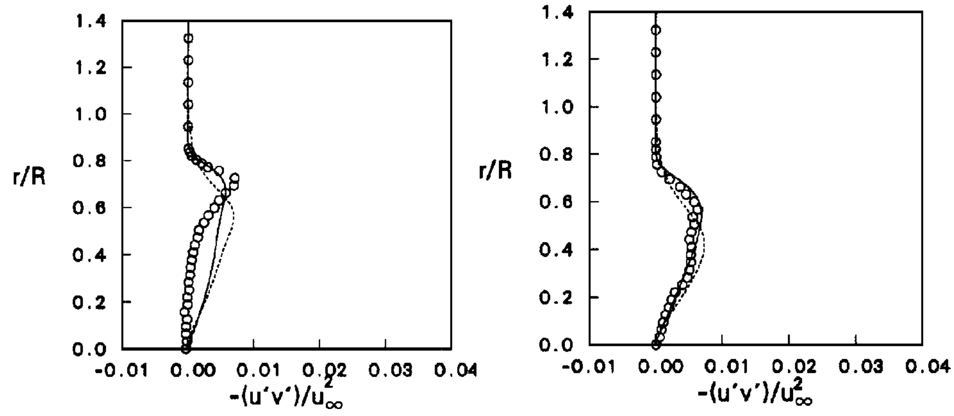

X/D = 0.95

X/D = 1.26

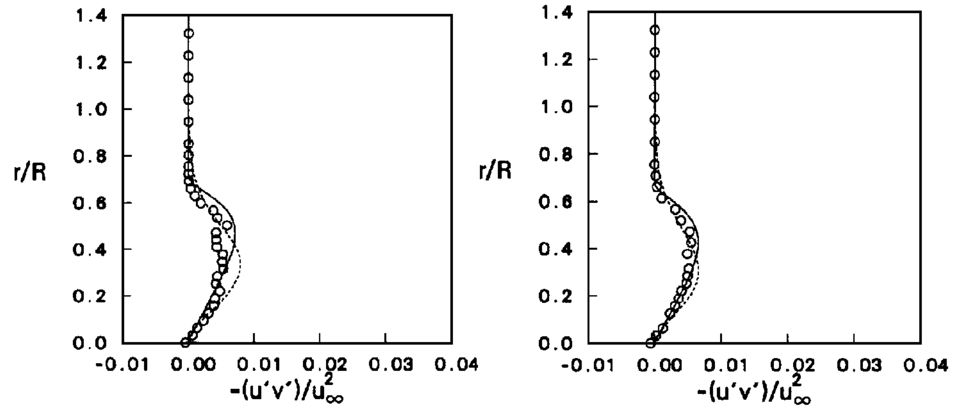

X/D = 1.67

X/D = 2.04

Fig. 10 Turbulent shear stress profiles; M_∞ = 2.46, α = 0, and I = 0.01: - - - -, B-L model; ——, k–ϵ model; and ○, experiment.

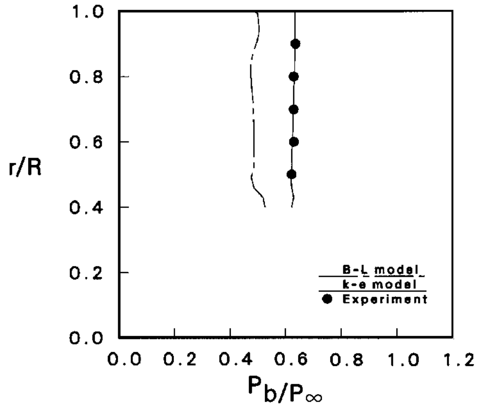

Fig. 11 Base pressure distribution; M_∞ = 2.46, α = 0, and I = 0.005.

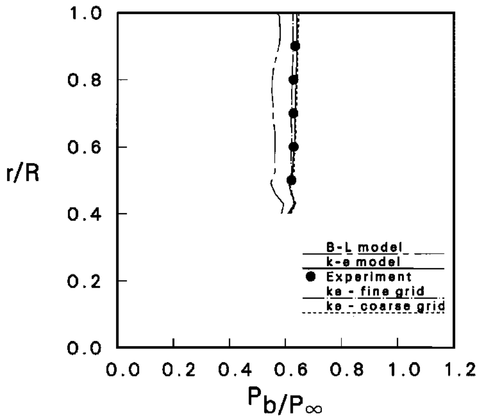

Fig. 12 Base pressure distribution; M_∞ = 2.46, α = 0, and I = 0.01.

Of particular interest is the accurate prediction of the base pressure and, hence, base drag. Figure 11 shows the base pressure distribution (along the base) for a mass injection rate, $I = 0.005$. The base pressures predicted by both the algebraic model and the two-equation k–ϵ turbulence model are compared with the experimental data.[11] The experimental data are shown in dark circles, and the computed results are shown in lines. Here, $r/R = 0.0$ corresponds to the centerline of symmetry, and $r/R = 1.0$ corresponds to the base corner. The base pressures predicted by both algebraic and k–ϵ turbulence models show almost no change in the radial base pressure distribution, which can also be observed in the experimental data. The base pressure magnitude is, however, poorly predicted by the algebraic model. A much improved base pressure distribution is predicted by the k–ϵ model, and its agreement with the measured base pressure is quite good. The algebraic model prediction shows slight radial variations near the base corner and the bleed exit corner. Figure 12 shows the base pressure distribution for an injection rate of $I = 0.01$. The computed base pressures obtained by both turbulence models are compared with the experimental data. Again the k–ϵ model predicted base pressure agrees well with the data, and the algebraic model prediction is poor. The grid sensitivity is examined in this figure using the results obtained by the k–ϵ model on three different grids (original medium, coarse, and fine). The coarse grid consists of half as many and the fine grid twice as many grid points as the original medium grid. The grid point distribution near the base also differs between these three grids. The y^+ values for the first point from the surface for these grids were 0.4, 1.4, and 8, respectively, for the fine, medium, and coarse grids. The difference in the computed base pressures obtained using the three grids is very small. Although not shown here, no significant changes were observed between the computed velocity profiles and the turbulent kinetic energy and turbulent shear stress profiles obtained using the three different grids. Computed results have also been obtained with the algebraic turbulence model on these grids and these results, which include base pressure, mean velocity profiles, and turbulent shear stress, also do not change appreciably with grid density. Thus, the computed solutions are grid independent, not only for the base

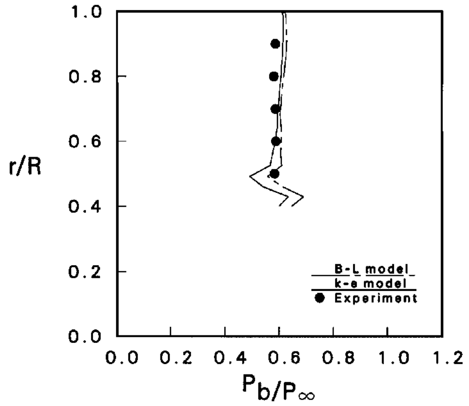

Fig. 13 **Base pressure distribution; M_∞ = 2.46, α = 0, and I = 0.028.**

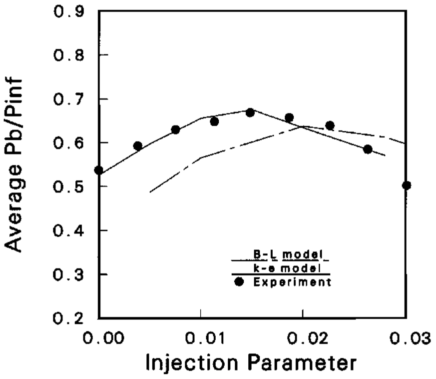

Fig. 14 **Effect of base bleed on average base pressure; M_∞ = 2.46 and α = 0.**

pressure but also for other mean and turbulent flow quantities in the near wake region. The base pressure comparison for a higher base bleed rate ($I = 0.028$) is shown in Fig. 13. The three grids again have very similar results in base pressure with the k–ϵ model. The base pressure distribution for the k–ϵ model is shown here for the medium grid. The predicted base pressure with the k–ϵ model agrees better with the experimental data than that predicted by the algebraic model. The wiggles seen near the bleed corner in the computed results can be attributed to the lack of grid clustering/alignment at the bleed corner. These wiggles can also be eliminated by the modeling of flow inside the bleed hole at very large bleed rates.

The effect of base bleed on radially averaged base pressure is shown in Fig. 14 as a function of mass injection parameter. The computed average base pressures predicted by both the algebraic and the k–ϵ model are compared with the experimental data. The algebraic turbulence model severely underpredicts the average base pressure for small mass injection rates. A much better average base pressure is predicted by the k–ϵ model, and its agreement with the measured average base pressure is quite good. The base pressure increases with the increase in the injection rate for low injection rates. This is the region where the base bleed is effective in increasing the base pressure and thereby reducing the base drag. The increase in base pressure with increasing injection rates occurs until the optimum bleed rate is reached. This optimum injection rate is approximately 0.015 as evidenced from the experimental data. The peak predicted by the k–ϵ model agrees well the data. The optimum peak value predicted by the algebraic model is near 0.02 and is not in good agreement with the data. With further increases in the injection rate from its optimum, the base pressure decreases, as evidenced by both experimental and computed results due to the onset of power-on flow conditions. A strong bleed jet shear layer and secondary recirculation region are formed, negating the benefits of base bleed.

Concluding Remarks

A zonal, implicit, time-marching Navier–Stokes computational technique has been used to compute the turbulent supersonic base flow over a cylindrical afterbody with base bleed. Flowfield computations have been performed at $M_\infty = 2.46$ and at a 0-deg angle of attack. Two eddy viscosity turbulence models (an algebraic and a two-equation k–ϵ) have been used to provide the turbulence closure. The k–ϵ equations are solved using an implicit algorithm, and calculations with the k–ϵ model are extended up to the wall.

Numerical results show the details of the flowfield in terms of Mach number contours. Comparisons of both the mean and turbulence quantities have been made with the available experimental data. The algebraic turbulence model predicts the mean velocity components poorly in the wake. In general, the velocity components predicted by the two-equation k–ϵ model are in better agreement with the experimental data than the algebraic model. Discrepancy exists between the predicted turbulent shear stress and the experiment for both algebraic and k–ϵ turbulence models in the recirculation region. An improvement in the predicted location and magnitude of the peak in shear stress is found with the k–ϵ model. Computed base pressure distributions have been compared with the measured base pressures. The base pressures are underpredicted by the algebraic model for different injection rates. The predicted base pressures for these injection rates with the k–ϵ model are found to be in good agreement with the experimentally measured base pressures.

References

[1] Sahu, J., Nietubicz, C. J., and Steger, J. L., "Navier–Stokes Computations of Projectile Base Flow With and Without Base Injection," U.S. Army Ballistic Research Lab., BRL-TR-02532, Aberdeen Proving Ground, MD, Nov. 1983; also see *AIAA Journal*, Vol. 23, No. 9, 1985, pp. 1348–1355.

[2] Sahu, J., "Supersonic Base Flow over Cylindrical Afterbodies with Base Bleed," AIAA Paper 86-0487, Jan. 1986.

[3] Sahu, J., "Computations of Supersonic Flow over a Missile Afterbody Containing an Exhaust Jet," *Journal of Spacecraft and Rockets*, Vol. 24, No. 5, 1987, pp. 403–410.

[4] Sahu, J., "Numerical Computations of Transonic Critical Aerodynamic Behavior," *AIAA Journal*, Vol. 28, No. 5, 1990, pp. 807–816.

[5] Sahu, J., and Nietubicz, C. J., "Three Dimensional Flow Calculation for a Projectile with Standard and Dome Bases," U.S. Army Ballistic Research Lab., BRL-TR-3150, Aberdeen Proving Ground, MD, Sept. 1990.

[6] Herrin, J. L., and Dutton, J. C., "Supersonic Base Flow Experiments in the Near-Wake of a Cylindrical Afterbody," *AIAA Journal*, Vol. 32, No. 1, 1994, pp. 77–83.

[7] Sahu, J., "Numerical Computations of Supersonic Base Flow with Special Emphasis on Turbulence Modeling," *AIAA Journal*, Vol. 32, No. 7, 1994, pp. 1547–1549.

[8] Bowman, J. E., and Clayden, W. A., "Cylindrical Afterbodies in Supersonic Flow with Gas Ejection," *AIAA Journal*, Vol. 5, No. 8, 1967, pp. 1524, 1525.

[9] Clayden, W. A., and Bowman, J. E., "Cylindrical Afterbodies at $M_\infty = 2$ with Hot Gas Ejection," *AIAA Journal*, Vol. 6, No. 12, 1968, pp. 2429–2431.

[10] Schilling, H., "Experimental Investigation on the Base-Bleed-Effect for Boat-Tail-Combinations," *Proceedings of the 8th International Symposium on Ballistics* (Amsterdam, The Netherlands), 1984.

[11] Mathur, T., and Dutton, J. C., "Base Bleed Experiments with a Cylindrical Afterbody in Supersonic Flow," AIAA Paper 95-0062, Jan. 1995.

[12] Pulliam, T. H., and Steger, J. L., "On Implicit Finite-Difference Simulations of Three-Dimensional Flow," *AIAA Journal*, Vol. 18, No. 2, 1982, pp. 159–167.

[13] Baldwin, B. S., and Lomax, H., "Thin Layer Approximation and Algebraic Model for Separated Turbulent Flows," AIAA Paper 78-257, Jan. 1978.

[14] Chien, K. Y., "Predictions of Channel and Boundary-Layer Flows with a Low-Reynolds-Number Turbulence Model," *AIAA Journal*, Vol. 20, No. 1, 1982, pp. 33–38.

[15] Jones, W. P., and Launder, B. E., "The Prediction of Laminarization with a Two-Equation Model of Turbulence," *International Journal of Heat and Mass Transfer*, Vol. 15, 1972.

[16] Sarkar, S., Erlebacher, G., Hussaini, M. Y., and Kreiss, H. O., "The Analysis and Modeling of Dilitational Terms in Compressible Turbulent Flows," *Journal of Fluid Mechanics*, Vol. 227, pp. 473–493.

[17] Sahu, J., and Danberg, J. E., "Navier–Stokes Computations of Transonic Flows with a Two-Equation Turbulence Model," *AIAA Journal*, Vol. 24, No. 11, 1986, pp. 1744–1751.

R. M. Cummings
Associate Editor